Energy barrier engineering of oxygen reduction reaction synergistically promoted by binary Zn-Cu pair sites for advanced Zn–air batteries

Mancai Qian [a],[1], Man Guo [a],[1], Yuan Qu [a], Meijiao Xu [a], Datai Liu [a], Cheng Hou [a],*,
Tayirjan Taylor Isimjan [b],*, Xiulin Yang [a],*

[a] Guangxi Key Laboratory of Low Carbon Energy Materials, School of Chemistry and Pharmaceutical Sciences, Guangxi Normal University, Guilin 541004, China
[b] Saudi Arabia Basic Industries Corporation (SABIC) at King Abdullah University of Science and Technology (KAUST), Thuwal 23955-6900, Saudi Arabia

ARTICLE INFO

ABSTRACT

Reducing the oxygen adsorption energy barrier is vital to accelerate the oxygen reduction reaction (ORR). Herein, we report a mesoporous cake-like structured Zn-N/Cu-N electrocatalyst (ZnCu-N-C) with robust electrocatalytic performance and exceptional durability in 0.1 M KOH solution. The mesoporous cake-like structure is promising to expose more active sites. Extended X-ray absorption fine spectroscopy and X-ray photoelectron spectroscopy confirmed the existence of M-N_x (M = Zn, Cu). More importantly, the density functional theory (DFT) calculations corroborate that the Zn-N/Cu-N dual active center can reduce the oxygen adsorption energy barrier. Therefore, the optimized ZnCu-N-C electrocatalyst is ahead of commercial Pt/C (20 wt%) in all aspects. Moreover, the ZnCu-N-C-based Zn–air batteries exhibit outstanding long-term stability of 240 cycles, a large power density of 156.2 mW cm^{-2}, and a high specific capacity of 732.7 mA h g^{-1}. This work may provide new guidance for the rational design of cathode catalysts in Zn-air batteries.

1. Introduction

The worldwide fossil energy shortage and relevant environmental issues require environmentally friendly, low-cost, and sustainable energy storage and conversion devices [1–4]. However, the high cost, insufficient energy density, and safety-concern limit its large-scale industrial applications [5]. The Zn-air batteries is regarded as one of the most promising due to the high theoretical specific energy density (1086 Wh kg^{-1}), low cost, and safety [6]. Consequently, the Zn-air batteries have been applied in navigation, traffic signal, and hearing devices [7,8]. The sluggish four-electron transfer reaction kinetics of the oxygen reduction electrocatalyst is the main reason that affects the performance of the Zn-air battery. To date, although Pt-group metal (PGM) electrocatalysts can efficiently address the kinetics-related issues, the unsatisfactory stability, high cost, and rare resource have significantly restricted its large-scale application [9–11]. As a result, attention has been drawn

to the development of alternative and low-cost catalysts, including: i) metal-free catalysts [12,13], ii) Fe-based or Co-based catalysts [1,14], and iii) transition metal (TM) oxide loading on nitrogen-doped carbon catalyst [15–17].

Recently, metal−organic frameworks (MOFs) and their derivatives have used as promising oxygen electrocatalysts, owing to their diverse metal centers/clusters and structural tailor ability [18,19]. Well-defined morphology and tunable chemical composition of MOFs make them efficient sacrificial templates and precursors for preparing desired nanomaterials [20,21]. Especially, zeolitic imidazolate frameworks (ZIFs) (such as ZIF-8) with TM-N_4 active sites are essential for multiple electrocatalytic reactions [22]. Nevertheless, materials derived from pyrolysis of MOFs precursors usually produce an aggregation of metal nanoparticles and micropores that are not efficient for reactants/products transfer, resulting in limited ORR performance [23]. Therefore, the development of efficient and durable TM-N-C electrocatalysts is an inevitable avenue to promote Zn-air batteries' performance.

Herein, we successfully synthesized zinc, copper- and nitrogen-doped mesoporous carbon cakes (denoted as ZnCu-N-C) via the pyrolysis of facial ZnCu-MOFs precursors. The density functional theory (DFT) calculations reveal that the Zn-N/Cu-N dual active centers reduce the oxygen adsorption energy barrier of ORR.

* Corresponding authors.
E-mail addresses: houcheng@gxnu.edu.cn (C. Hou),
isimjant@sabic.com (T.T. Isimjan), xlyang@gxnu.edu.cn (X. Yang).
[1] These authors contributed equally to this work.

Specifically, the catalyst ZnCu-N-C obtained at 1000 °C exhibited an outstanding activity with an $E_{1/2}$ of 0.87 V (vs. RHE) in alkaline medium, as well as superior stability (relative current only decayed by 3.6% after 40,000 s), outperforming commercial Pt/C. Furthermore, the ZnCu-N-C-driven Zn-air batteries delivered a power density of 156.2 mW cm^{-2} and a specific capacity of 732.7 mAh g^{-1} higher than those of commercial Pt/C. The Zn-air batteries assembled with ZnCu-N-C + RuO$_2$ as an air cathode have no significant attenuation in continuous operation for 130 h, which proves its potential application prospects in metal-air battery.

2. Experimental section

2.1. Materials

All chemicals and solvents were used directly without any further purification. Methanol (AR, 99.5%), ethanol (AR, 99.7%), potassium hydroxide (AR) was purchased from Xilong chemical Co., Ltd. Benzimidazole (AR, 98.0%) was bought from Aladdin Industrial Corporation. Zinc nitrate hyexahdrate (AR) and copper (II) sulfate pentahydrate (AR) were purchased from Sinopharm Chemical Reagent Co., Ltd. Nafion solution (5 wt%) was purchased from Alfa Aesar. Commercial Pt/C (20 wt% Pt) was bought from Macklin Biochemical Co., Ltd. (Shanghai, China). Deionized water was used for all experiments.

2.2. Synthesis of ZnCu-N-C catalysts

In a typical synthesis process, Copper (II) sulfate pentahydrate and zinc nitrate hyexahdrate and (molar ratio of 1: 20, the amount of total metal salt keeping at 2.54 mmol), 10 mmol benzimidazole (BIM) were dissolved in 30 mL mixed solvent of ethanol and DI water (V: V = 1: 1) with ultrasonication to form solution A and B, respectively. Subsequently, solution A was added into solution B drop by drop under magnetic stirring. After 24 h, the sample was collected by centrifugation and washed with ethanol, then dried in an oven at 70 °C for overnight. The obtained ZnCu-MOF powder was calcined at different temperature (900, 1000, 1100 °C) for 2 h under Ar atmosphere. The product was collected after cooling to room temperature is designated as ZnCu-N-C (T) (T = 900, 1000, 1100).

For comparison, the catalysts were prepared by altering the molar ratio of Cu/Zn by adjusting ratio of the metal salt to 1/10, 1/30, and 1/50, respectively. The obtained samples with different mole ratio were named as x-ZnCu-N-C. The Zn-N-C catalysts were achieved by annealing Zn-ZIF at 1000 °C under nitrogen atmosphere. Unless otherwise stated, the ZnCu-N-C discussed below refers to the Zn/Cu precursor calcined at 1000 °C with a molar ratio of Cu to Zn is 1/20.

2.3. Zn-air batteries fabrication

Zn-Air battery measurements were carried out in a homemade battery. 2 mg of ZnCu-N-C catalyst was ultrasonically dispersed into a mixed solution of 150 μL of water, 5 μL of 5 wt% Nafion, and 50 μL of isopropanol to prepare the catalyst ink. The obtained slurry was coated on carbon paper (~1 mg cm^{-2}) as a gas diffusion layer. Zn plate was served as the anode, and a mixed solution of 0.2 M Zn(Ac)$_2$ and 6.0 M KOH was used as the electrolyte to assemble a Zn-air battery. Furthermore, the mixed catalyst slurry of ZnCu-N-C + RuO$_2$ with a mass ratio of 1:1 was used as an air cathode during the stability test. For comparison, Pt/C + RuO$_2$ was tested using the same method. An electrochemical workstation (CHE 760E) was used to carry out the polarization curve and open circuit voltage (OCV) of Zn-air battery, and the stability was recorded with a LAND battery test system (BT2016A) at a current density of 5 mA cm^{-2}. Each charge and discharge period were set to be 10 min. As a comparison,

Zn-air battery based on benchmark Pt/C was measured under the same case.

2.4. Electrochemical measurements

The LSV curves and chronoamperometry responses were recorded on an electrochemical workstation (Pine Research Instrumentation, Inc., Durham, NC, USA). A rotating ring-disk electrode (RRDE) with 5.61 mm in diameter was served as the working electrode. The Ag/AgCl (sat. KCl) and a graphite rod are used as reference and counter electrodes, respectively. All the potential values were calibrated for the reversible hydrogen electrode (RHE) according to the following equation: E (vs. RHE) = E (vs. Ag/AgCl) + 0.961 V (Fig. S1).

Before the modification, the working electrode was polished with 0.05 μL alumina powder and rinsed with water, 0.5 M H$_2$SO$_4$, and ethanol 3 times, respectively. The catalyst inks were prepared by ultrasonically dispersing the catalyst (4.0 mg) in 1 mL mixed solvent of 500 μL isopropanol and 500 μL deionized water in the presence of 5 wt% Nafion. For the working electrode, the loading of the ZnCu-N-C catalyst is 0.318 mg cm^{-2}, while the loading of a commercial Pt/C (20 wt% Pt, JM) is 0.081 mg cm^{-2}. The ORR activity was evaluated in O$_2$- or N$_2$-saturated 0.1 M NaOH solution at a scan rate of 10 mV s^{-1} with varying rotating speeds from 400 to 2500 rpm.

The hydrogen peroxide yield was determined by rotating ring disk electrode (RRDE) measurement with a disk electrode (Pine Research Instrumentation, S$_{disk}$ = 0.247 cm^2) and a ring electrode (Pt electrode, area 0.1858 cm^2). The scan rate of the disk electrode was 10 mV s^{-1}, and the ring electrode potential was 1.2 V (vs. RHE).

The stability tests were carried out using the chronoamperometric technique at the rotation rate of 1600 rpm in O$_2$-saturated electrolyte for 35,000 s. The methanol crossover effects in CVs were recorded by adding 3.0 M methanol into the O$_2$-saturated 0.1 M KOH. The methanol poisoning measurements were also recorded by the chronoamperometric response in O$_2$-saturated KOH solution at the rotation speed of 1600 rpm, adding 3.0 M methanol at 200 s

To calculate the electrochemical double-layer capacitance (C_{dl}), the electrode potential is scanned between 0.12 and 0.24 V (vs. Ag/AgCl) at different scan rates (8–24 mV s^{-1}). The specific capacitance can be converted into an electrochemical active surface area (ECSA) using the specific capacitance value of a flat 1 cm^2 of real surface area. The capacitance of a flat surface is generally observed to be between 20 and 60 mF cm^{-2} [24,25].

2.5. Computational models and methods

The DFT calculations were performed using the Vienna ab initio Simulation Package (VASP). The projected augmented wave (PAW) method was adopted to describe the electron-ion interactions. The Perdew-Burke-Ernzerhof (PBE) exchange-correlation functional within the generalized gradient approximation (GGA) was employed. We employed a graphene supercell with a surface periodicity of 5 × 5 as a basis. The Brillouin zone was sampled by the 2 × 2 × 1 Gamma-centered k-point mesh. The plane-wave kinetic cutoff energy was set to be 500 eV. The convergence tolerance of energy of 1.0 × 10^{-5} eV/atom and maximum force of 0.05 eV/Å are employed in all the geometry optimizations. A vacuum of 30 Å was included to isolate the interaction between each sheet. All atoms were fully relaxed in structural optimization and have been confirmed to be the minimum with no imaginary frequencies. In alkaline medium, the 4e$^-$ ORR mechanism can be expressed as follows:

$$* + O_2 \rightarrow {}^*O_2 \tag{1}$$

$$^*O_2 + H_2O + e^- \rightarrow {}^*OOH + OH^- \tag{2}$$
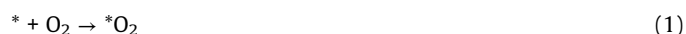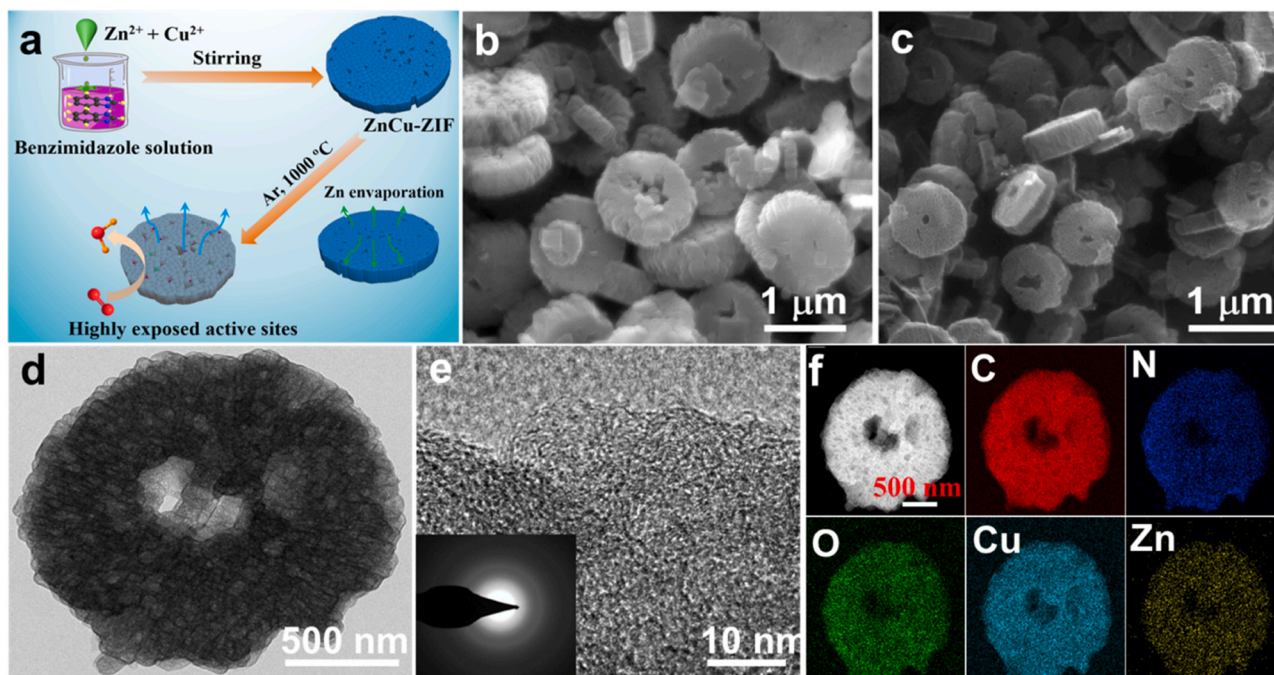
Fig. 1. (a) Illustration of the synthesis of gradient ZnCu-N-C. SEM images of (b) ZnCu-ZIF and (c) ZnCu-N-C. (d) TEM, (e) HR-TEM images (inset: SAED pattern), and (f) the corresponding element mappings of ZnCu-N-C.

$$*OOH + e^- \rightarrow *O + OH^- \tag{3}$$

$$*O + H_2O + e^- \rightarrow OH^- + *OH \tag{4}$$

$$*OH + e^- \rightarrow * + OH^- \tag{5}$$

Where * represents an active site on the catalyst surface, the electrochemical processes are investigated using the computational hydrogen electrode (CHE) method developed by Norskov et al. [26]. The ΔG value is determined as follows:

$$\Delta G = \Delta E + \Delta ZPE - T\Delta S + \Delta G_{pH} + eU \tag{6}$$

Where ΔE is the electronic energy difference obtained from DFT calculations, ΔZPE is the change in zero-point energies calculated from the vibrational frequencies, T is the temperature (T = 298.15 K), and ΔS is the entropy change. ΔG_{pH} is the correction of the OH^- free energy by the concentration, which can be determined as ΔG_{pH} = 2.303 × kBT × pH (or 0.059 × pH), where kB is the Boltzmann constant. The pH value was assumed to be 13. The terms e and U are the number of electrons transferred and the applied electrode potential, respectively. The free energy at the starting point of the catalytic cycle is set to 0 eV, and under the condition of pH= 13, the total reaction free energy is − 1.84 eV. For each elementary step, the Gibbs free energy was calculated at the standard conditions (U = 0 V).

3. Results and discussion

3.1. Synthesis strategy and microstructure analysis

Fig. 1a illustrates the preparation process of ZnCu-N-C by calcination of Zn/Cu bimetallic ZIF. ZnCu-ZIF was synthetized by stirring the $Zn(NO_3)_2$, $CuSO_4$ and benzimidazole (BIM) in a mixed solvent of ethanol and DI water at room temperature. According to previous reports, bimetallic MOFs (e.g., Zn/Co-MOFs, Co/Cu-MOFs, Co/Ni-MOFs) possess a relatively uniformity composition of metal active

sites [27,28]. Similarly, Cu and Zn species are also uniformly distributed throughout the CuZn-ZIF framework, and no agglomeration was observed in this work (Fig. S2a). Further investigation of the morphology suggested that the introduction Cu^{2+} does not affect the ZIF structure. The SEM images of Zn-ZIF and ZnCu-ZIF materials display the similar cake-like morphology (Fig. S2b-c). The powder XRD pattern (Fig. S2d) shows that ZnCu-ZIF and Zn-ZIF have similar crystal phases, and are basically consistent with the literature [29].

The morphologies of ZnCu-N-C were depicted in the images obtained from scanning electron microscopy (SEM) and transmission electron microscopy (TEM). The SEM images show that the obtained ZnCu-ZIF has a cake-like structure (Fig. 1b), and the morphology changes little after being calcined at a temperature of 1000 °C (Fig. 1c). The TEM image in Fig. 1d confirmed the well-defined cake-like architecture with pores. The high-resolution TEM image (Fig. 1e) revealed the ZnCu-N-C has no obvious lattice fringes and is mainly composed of amorphous architecture. There is no obvious bright ring in the selected area electron diffraction (SAED) image, which further confirms its amorphous characteristics (inset Fig. 1e). The corresponding element mapping confirmed the ZnCu-N-C contain C, N, O, Cu and Zn element and all elements are uniformly distributed throughout the cake-like structure (Fig. 1f). The EDS spectrum further verified the coexistence of C, N, O, Cu and Zn element in the composites (Fig. S3). The Zn and Cu contents in all samples were measured by inductively coupled plasma optical emission spectrometry (ICP-OES) (Table S2). We detected that the content of Zn and Cu in the ZnCu-N-C (20:1) is 0.55 wt% and 1.20 wt%, respectively.

The XRD pattern of the ZnCu-N-C shows two typical diffraction peaks for graphitic carbon (JCPDS no. 26-1079) (Fig. 2a) [30]. As for Zn-N-C, the XRD pattern shows only diffraction for graphitic carbon, while no other diffraction can be detected. This result is accordance with the SAED result. The Raman spectra of x-ZnCu-N-C and ZnCu-N-C (T) catalysts exhibit D bands at 1335 cm^{-1} and G bands at 1580 cm^{-1} typical feature of graphitic carbon with structural defects [31]. The ZnCu-N-C show a relatively low I_D/I_G ratio of 0.94, much lower than that of Zn-N-C (Fig. 2b). Interestingly, ZnCu-N-C has a lower degree of graphitization compared with x-ZnCu-N-C (x = 10:1, 30:1, 50:1) (Fig. S4a). Notably, the graphitization degrees of all
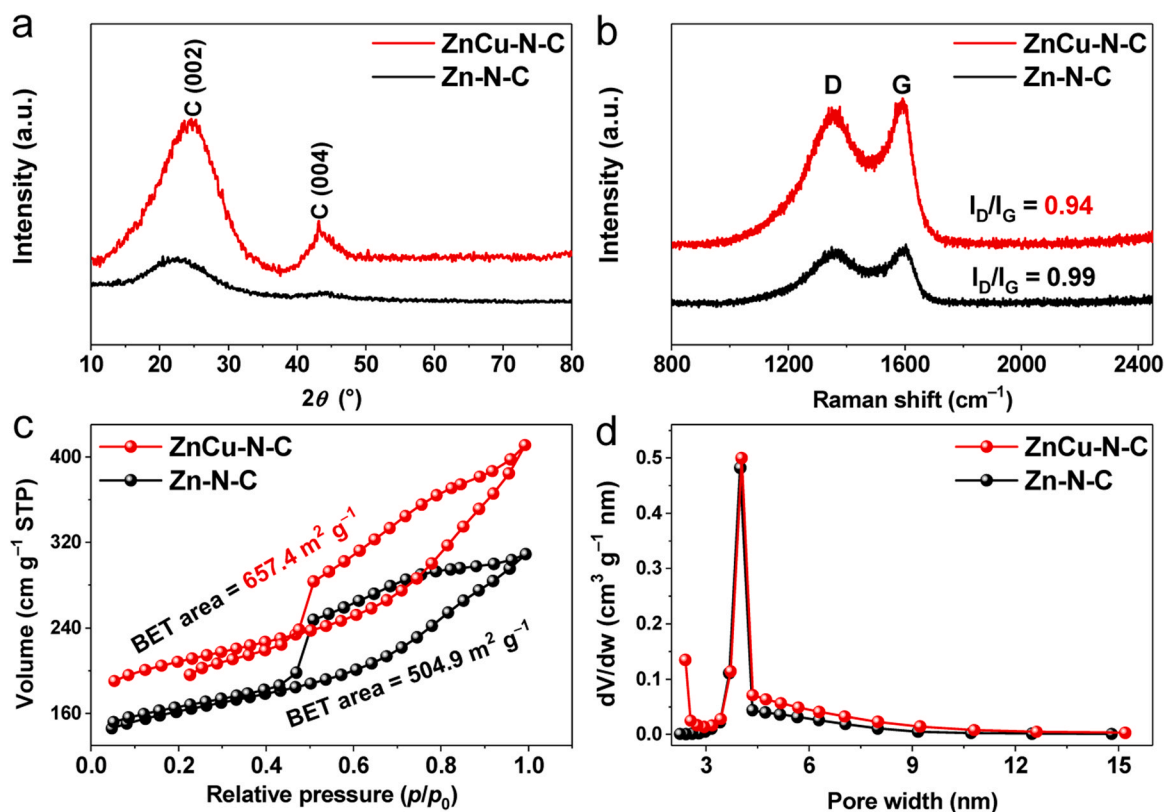
Fig. 2. (a) XRD patterns, (b) Raman spectra, (c) Nitrogen adsorption-desorption isotherms and (d) pore size distributions of ZnCu-N-C and Zn-N-C.

samples are very close. In addition, the ratio of I_D/I_G decreases with increasing temperature from 0.97 to 0.92 (Fig. S4b). A lower I_D/I_G value confirms a higher degree of carbonization, which is usually accompanied by more severe metal reduction and loss of N dopants.

The BET surface areas of ZnCu-N-C and Zn-N-C are 657.4 m^2 g^{-1} and 504.9 m^2 g^{-1}, respectively. The similar isotherms for ZnCu-N-C and Zn-N-C at low pressure indicate a similar mesoporous structure (Fig. 2c). Meanwhile, the pore size distribution curves (Fig. 2d) illustrate that both ZnCu-N-C and Zn-N-C have abundant mesoporous structures in the pyrolysis process and the pore size is about 5.0 nm. These results indicate that the pyrolysis of ZIF can increase the specific surface area similar to the previous literature [32,33]. Studies have found that the mesopores are formed by the sublimation of Zn species in the ZnCu-MOF structure.

The thermal stability of the prepared ZnCu-ZIF was investigated by thermogravimetric analysis (TGA) and the corresponding result is presented in Fig. S5. The TGA curve shows a weight loss (7.9%) up to 330 °C, which can be attributed to the collapse of framework. A strong exothermic peak appeared at 719.2 °C due to decomposition of the benzimidazolate fragment and resulting in formation of nitrogen doped carbon. There is a small exothermic peak appeared at 789.4 °C, which can be attributed to the evaporation of Zn in the ZnCu-ZIF. TG analysis indicated that ZnCu-ZIF is an excellent precursor for synthesis of Zn-Cu-N co-doped carbon catalyst due to high thermal stability.

3.2. Chemical State and Active Site Analysis

XPS measurements were conducted to reveal the surface element composition and chemical state of ZnCu-N-C and Zn-N-C materials (Fig. 3). The survey spectrum in Fig. 3a approves the co-existence of C, N, O, Cu and Zn in the ZnCu-N-C catalyst. The carbon species can be fitted into four types: C=C, C-C/C-N, C−O and C=O bonds (Fig. S6)

[34,35]. The high-resolution N 1 *s* spectrum (Fig. 3b) can be deconvoluted into four peaks pyridinic-N (397.8 eV), pyrrolic-N (400.5 eV), graphitic-N (403.6 eV), oxidized-N (406.5 eV), and M-N_x (M = Cu, Zn) (399.1 eV) [36,37], indicating that the successful formation of M-N_x sites. Notably, the content of pyridinic-N and M-N_x in ZnCu-N-C is significantly higher than that of Zn-N-C (Fig. 3b). Importantly, the pyridinic-N and M-N_x (M = Zn, Cu) have been demonstrated as the active sites during ORR [38,39]. The high resolution Zn 2*p* spectrum exhibits two distinct peaks ascribable to Zn $2p_{1/2}$ (1044.5 eV), and Zn $2p_{3/2}$ (1021.3 eV) (Fig. 3c) [40]. In Cu 2*p* spectrum, the peaks located at 932.2 and 952.4 eV can be attributed to Cu $2p_{3/2}$ and Cu $2p_{1/2}$, respectively [41]. One should note that the Cu (0) is unavoidable since carbon species can reduce the Cu ions at high-temperature (Fig. 3d), which contributes to the improvement of material conductivity [42]. The other two peaks at 934.8 and 955.0 eV can be assigned to Cu^{2+}, which coordinates with N atom to form Cu-N_x active sites.

Synchrotron radiation-based X-ray absorption spectroscopy, with high sensitivity to electronic and geometric structures, was used to reveal the structure of active sites. Fig. 3e shows the K-edge XANES spectrum of ZnCu-N-C and Zn foil as the references. The Fourier-transformed (FT) k^3-weighted (FT-EXAFS) curves of ZnCu-N-C show a prominent peak at approximately 1.50 Å, which is mainly assigned to the first shell Zn-N coordination [43]. In contrast to the case of Zn foil, no peak belonging to Zn-Zn bond was detected at around 2.30 Å. In addition, the FT-EXAFS spectrum of the ZnCu-N-C shows that there are two main peaks at about 1.53 and 2.15 Å, which are attributed to Cu-N and Cu-Cu coordination, respectively (Fig. 3f) [44]. Among them, the Cu-Cu coordination is consistent with the theoretical results in Cu foil. Most studies have confirmed that Zn-N and Cu-N with single atom structure are the main active sites of ZnCu-N-C catalysts used in catalytic ORR [45,46].
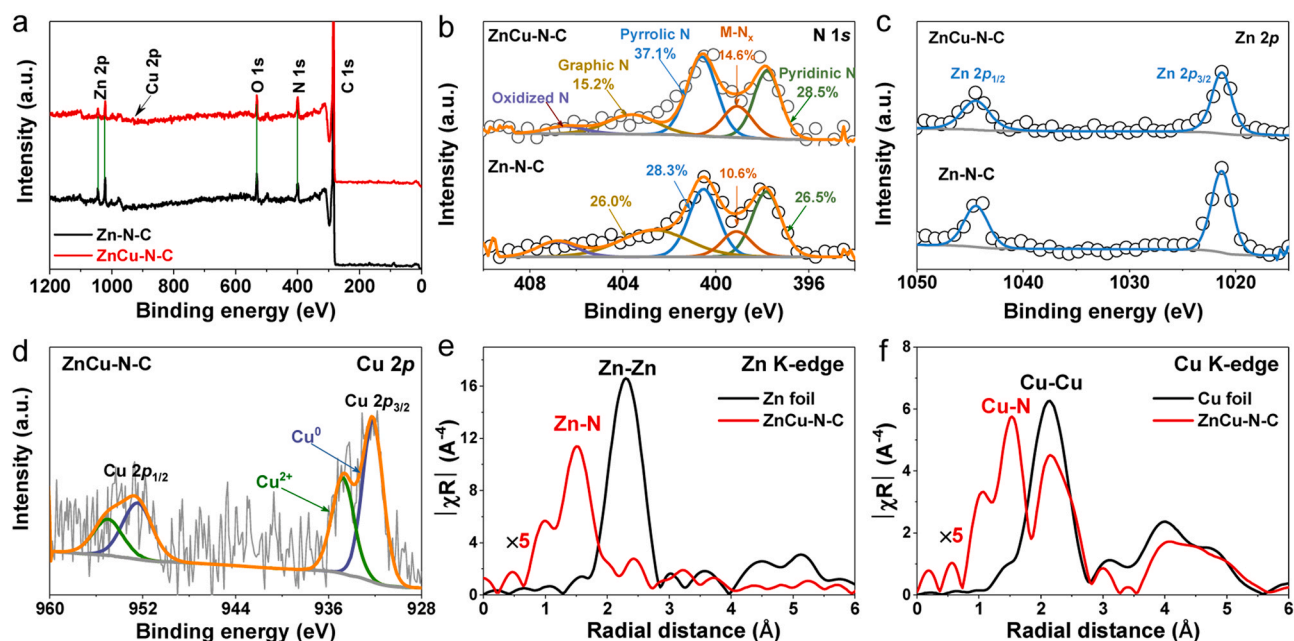
Fig. 3. (a) XPS survey spectra, (b) high-resolution N 1*s* spectra, (c) Zn 2*p* spectrum, and (d) Cu 2*p* of ZnCu-N-C and Zn-N-C. Fourier transformed EXAFS spectra of the (e) Zn *K* edge and (f) Cu *K* edge for Zn foil, Cu foil and ZnCu-NC, respectively.

3.3. Electrochemical analysis

The ORR performance was tested in 0.1 M KOH. First, the electro-catalytic active of ZnCu-N-C catalysts prepared at different annealing temperatures were discussed by cyclic voltammetry (CV) in O_2- or N_2-saturated 0.1 M KOH solution. As depicted in Fig. S7a, the CV curves of all catalysts in N_2-saturated electrolyte were virtually featureless, while clear cathodic peaks appeared in O_2-saturated electrolyte. Among them,

ZnCu-N-C (1000) showed the highest positive peak potential (0.81 V), which indicated perform the best ORR activity. Meanwhile, ZnCu-N-C (1000) displayed most positive half-wave potential ($E_{1/2}$ = 0.87 V) (Fig. S7b). The above results indicate that the appropriate pyrolysis temperature is essential for the enhancement of ORR activity. Furthermore, the Cu/Zn molar ratio is another important factor affecting the ORR performance. The ZnCu-N-C showed the best ORR activity when the Cu/Zn molar ratio was 1/20 (Fig. S8).
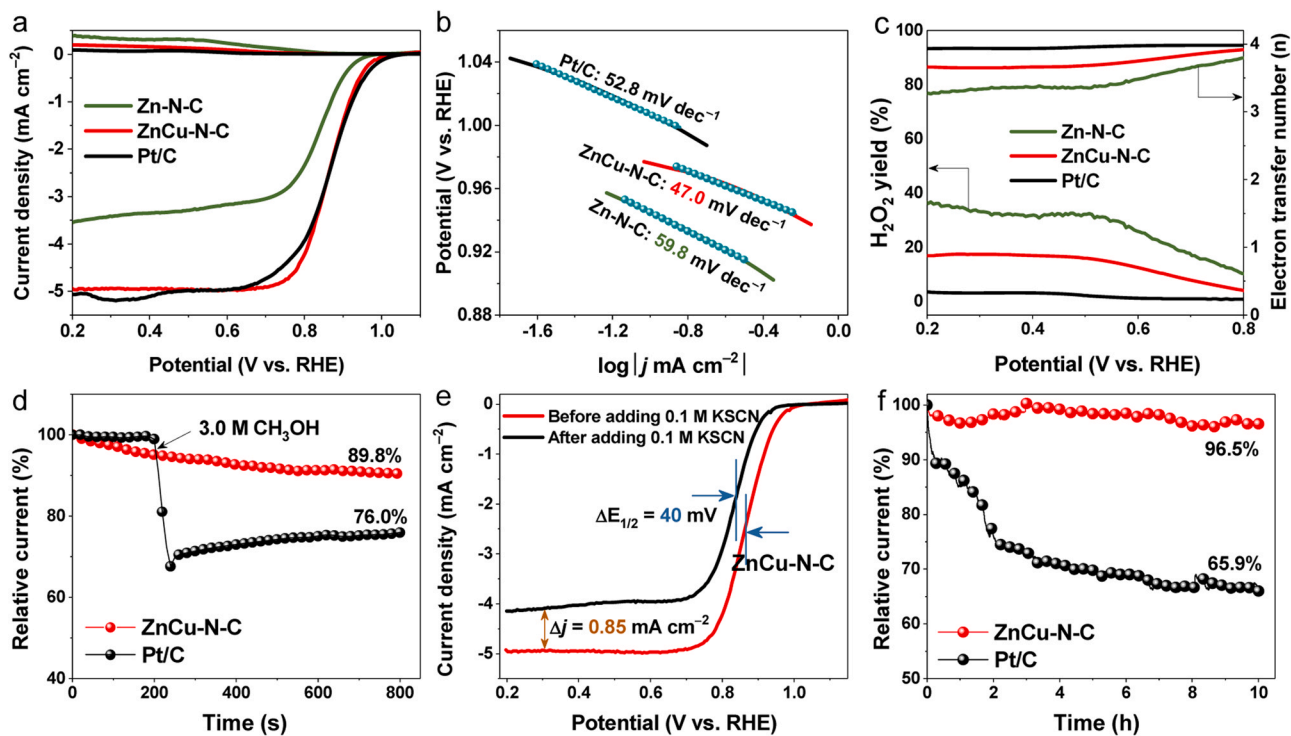
Fig. 4. (a) RRDE curves and (b) Tafel slope of catalysts. (c) Corresponding H_2O_2 yield and *n* for ZnCu-N-C, Zn-N-C and Pt/C catalysts. (d) Methanol tolerance tests for ZnCu-N-C and commercial Pt/C upon addition of 3.0 M methanol. (e) LSVs of ZnCu-N-C before and after the addition of 0.1 M KSCN in O_2-saturated 0.1 M KOH. (f) Normalized chron-oamperometry curves for the ZnCu-N-C and commercial Pt/C, respectively.
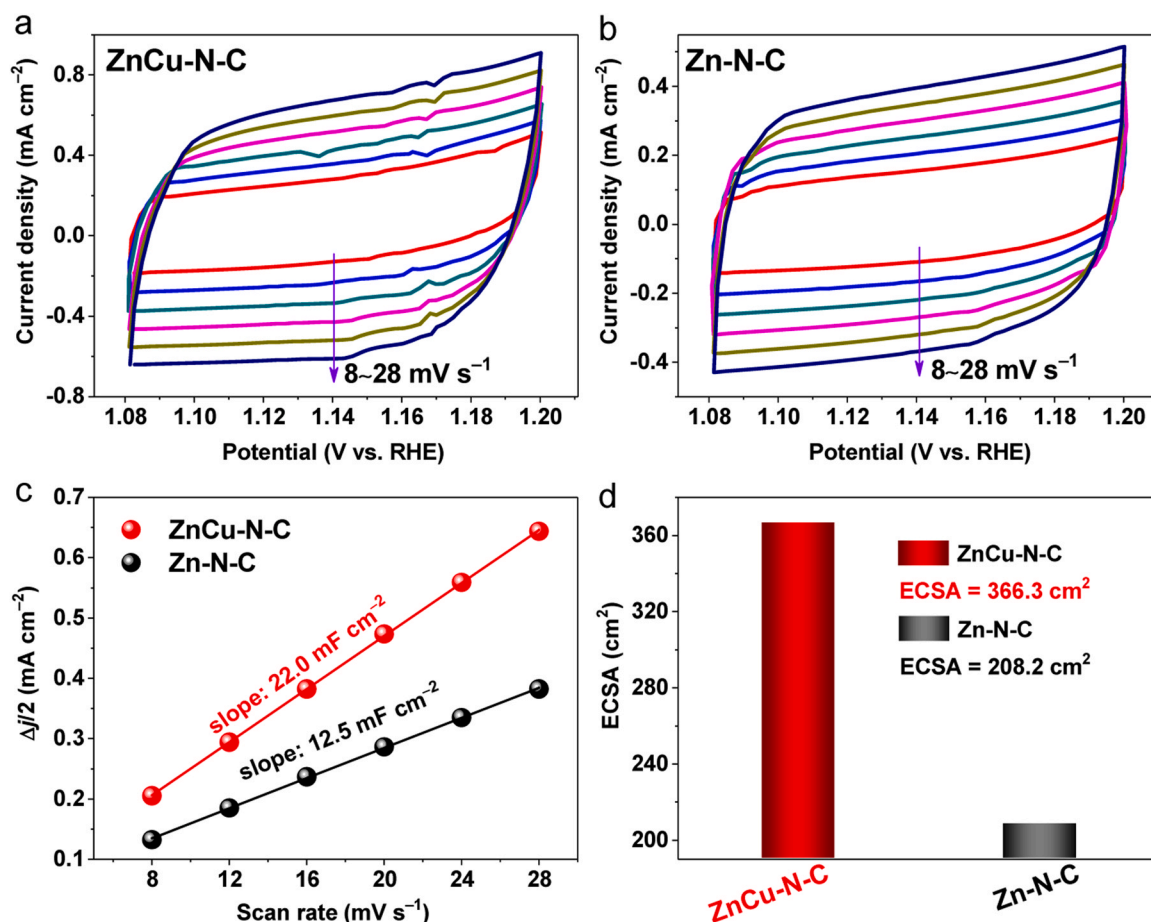
Fig. 5. CV curves of (a) ZnCu-N-C and (b) Zn-N-C at different scan rates. (c) Corresponding current density as function of scan rates of ZnCu-N-C and Zn-N-C for calculating the C_{dl}. (d) Corresponding ECSA for ZnCu-N-C and Zn-N-C, respectively.

The ORR performance of ZnCu-N-C and Zn-N-C was investigated in alkaline media. The RRDE test results attested the high ORR performance of the ZnCu-N-C (Fig. 4a). It shows higher half-wave potential (0.87 V vs. RHE) as well as larger diffusion-limited current density (5.00 mA cm^{-2} at 0.3 V) and kinetic current density (J_k: 2.62 mA cm^{-2} at 0.9 V) than those values of Zn-N-C and surpassed that of Pt/C (Table S3), and most of MOF-derived catalysts reported in recent literatures (Table S4). Furthermore, ZnCu-N-C exhibits a lower Tafel slope (47.0 mV dec^{-1}) compared to Pt/C (52.8 mV dec^{-1}), indicating that it possessed faster ORR reaction kinetics (Fig. 4b) [47]. The yields of H$_2$O$_2$ (%) for ZnCu-N-C is lower than that of Zn-N-C, and the electron transfer number (n) of ZnCu-N-C is calculated to be approximately 3.8, confirming the effective four-electron ORR pathway (Fig. 4c) [48,49]. This result indicated that Cu played a vital role in the improvement of ORR activity and Cu-Cu bonds acts as a synergistic promotor during electrocatalysis [50].

The excellent methanol tolerance and robust stability of electrocatalysts are of great significance for the commercialization of fuel cell technology. As shown in Fig. 4d, the ZnCu-N-C indicated outstanding tolerance to methanol crossover with negligible deviation of current density upon the rapid injection of methanol. In additional, it is established that the SCN$^-$ ion has a high affinity to transition metal compounds and can poison Cu-N/Zn-N coordination sites [51,52]. As shown in Fig. 4e, the E$_{1/2}$ of ZnCu-N-C catalyst is negative shifted by 40 mV and the limiting current density is severely after the introduction of SCN$^-$ ions, confirming that the Cu-N/Zn-N species are regarded as active sites in the ORR process. The electrochemical stability of ZnCu-N-C is evaluated in O$_2$-saturated 0.1 M KOH by chronoamperometry at 0.5 V. As shown in Fig. 4f, the ZnCu-N-C emerged

superb stability with the current retention of 96.4% superior to that of Pt/C (34.1%) after 40,000 s continuous operation.

The TEM and HAADF-STEM image of ZnCu-N-C after stability measurement in Fig. S9 further demonstrates the excellent stability of ZnCu-N-C. The corresponding element mapping shows that the uniform distribution of Zn and Cu. The above results confirm that Zn and Cu element did not accumulate after the stability test, which further verifies that the ZnCu-N-C catalyst has outstanding stability.

As discussed above, the ZnCu-N-C with mesoporous structure increases the electroactive surface area of the catalyst. To further demonstrate this point, we measured the capacitance of ZnCu-N-C and Zn-N-C to evaluate the electrochemical double layer capacitance (C_{dl}) for ORR (Fig. 5a and b). Based on the current density at different scan rates, the calculated C_{dl} was 21.98 mF cm^{-2} for ZnCu-N-C (Fig. 5c), which is 1.76-fold higher than that of Zn-N-C, indicating a large ECSA for ZnCu-N-C catalyst. Correspondingly, the calculated ECSA of ZnCu-N-C and Zn-N-C is 366.33 and 208.17 cm^2, respectively (Fig. 5d).

3.4. DFT theoretical calculation

To illuminate on the origin of the observed activity difference, density functional theory calculation (DFT) was carried out. The 4e$^-$ associative mechanism (O$_2$ → OOH → O → OH → H$_2$O) is proposed in Fig. 6a according to relevant studies [53]. The free energy diagrams of the ORR process on mono-site and dual-site centers are depicted in Fig. 6b. The DFT calculation results suggest that the adsorption energy of oxygen is − 0.23 eV, 0.50 eV and 0.18 eV for ZnCuN$_6$, ZnN$_4$ and CuN$_4$, respectively, confirming that the bimetallic active sites significantly reduce the adsorption energy barrier. Moreover, it is
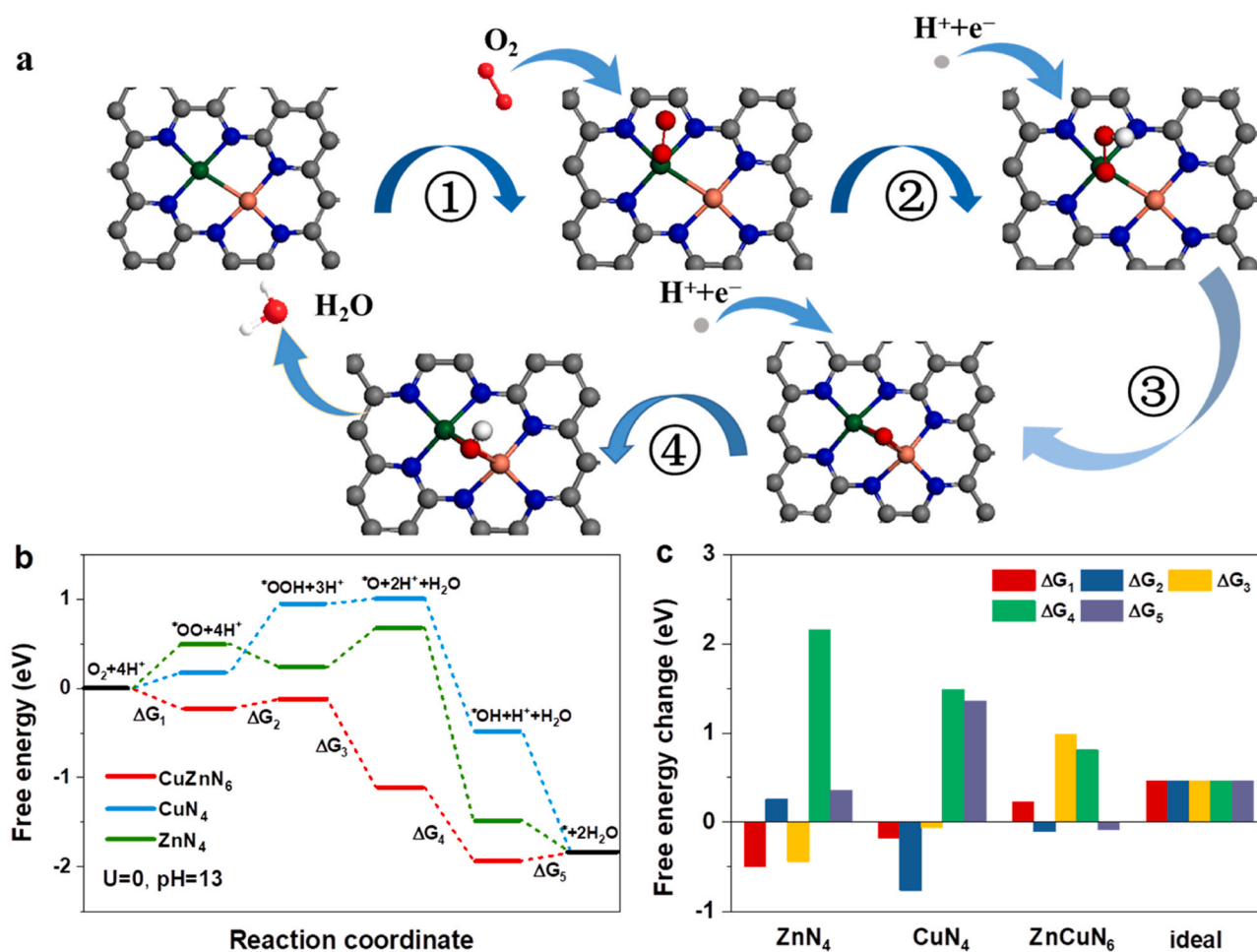
Fig. 6. (a) Proposed ORR mechanism, (b) free energy diagram, and (c) energy changes of four-electron pathway on mono-site and dual-site centers.
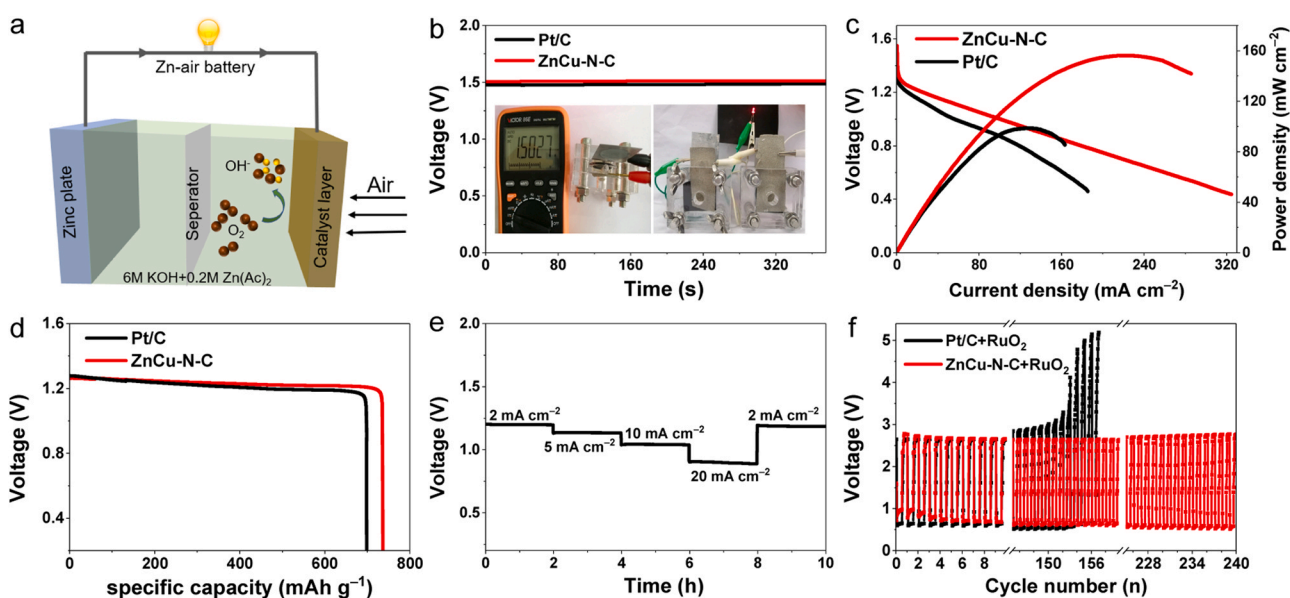
Fig. 7. (a) Schematic diagram of an aqueous Zn-air battery. (b) Open-circuit voltage of Zn-air batteries. (c) Polarization curves and power density plots. (d) Specific capacities of ZnCu-N-C and Pt/C based Zn-air batteries at current density of 10 mA cm^{-2}. (e) Discharge curves of Zn-air batteries containing ZnCu-N-C and PSt/C electrocatalysts at various current densities in the range of 2–20 mA cm^{-2}. (f) Galvanostatic discharge-charge cycling curves at 5.0 mA cm^{-2} of the liquid Zn-air batteries.

shown that the formation processes of metal-oxo intermediate are endothermic in ZnN_4 ($\Delta G_O = 0.68$ eV) and CuN_4 ($\Delta G_O = 1.01$ eV) systems, which is in sharp contrast to the exothermic process in $ZnCuN_6$ catalyst ($\Delta G_O = -1.12$ eV). With the aid of extra active site, the $ZnCuN_6$ catalyst effectively stabilizes the metal-oxo intermediate via the bimetal bridge mode, providing a strong driving force for the catalytic cycle. The free energy barriers of each step of the dual $ZnCuN_6$ catalyst are relatively average compared with ZnN_4 and CuN_4 catalysts (Fig. 6c and Table S1). Thus, the theoretical estimated overpotential (η) is 0.56 V, 0.90 V and 1.22 V, for $ZnCuN_6$, ZnN_4 and CuN_4, respectively, suggesting the $ZnCuN_6$ catalyst exhibits the best catalytic activity, which is in line with the experimental observation.

3.5. The performance of Zn-Air Batteries (ZABs)

The Zn-air batteries (ZABs) were tested in order to verify the practical application prospects of ZnCu-N-C catalyst. Fig. 7a shows the schematic diagram of the Zn-air battery, the Zn plate and 6 M KOH + 0.2 M $Zn(Ac)_2$ applied as the anode and the electrolyte, respectively. The open circuit voltage (OCV) of ZnCu-N-C (1.51 V) is higher than benchmark Pt/C (1.48 V). Moreover, the OCV of ZnCu-N-C is also measured by using a multimeter, suggesting its excellent electrocatalytic activity. Interestingly, two ZABs connected in series can successfully lit up an LED light (inset in Fig. 7b). As shown in Fig. 7c, ZABs were driven by ZnCu-N-C exhibit a power density of 156.2 mW cm^{-2}, which was distinctly higher than that of Pt/C (128.6 mW cm^{-2}). The above results indicate that ZABs emerges good performance by using ZnCu-N-C catalyst as an air cathode. The specific capacities of ZnCu-N-C based ZABs is calculated to be as high as 732.7 mA h g^{-1} when discharged at 10 mA cm^{-2}, which is higher than that of Pt/C (692.0 mA h g^{-1}) (Fig. 7d). The rate performance of ZABs was evaluated by discharging at different current densities such as 2, 5, 10, 20 mA cm^{-2} (Fig. 7e). ZABs is driven by ZnCu-N-C exhibited the superb rate performance with the voltage retention of 99.2% at 2 mA cm^{-2}. The admirable performance of ZABs based on ZnCu-N-C is consistent with its enhanced ORR kinetics and electrocatalytic capabilities. As depicted in Fig. 7f, the discharge and charge curves obtained for ZnCu-N-C + RuO_2 is almost no degradation after 240 continuous cycles compared to Pt/C + RuO_2. The above results suggested that the cake-like ZnCu-N-C material possessed outstanding ORR activity and stability, and it has a potential application prospect in metal-air batteries.

4. Conclusions

In summary, we have put forward the controlled pyrolysis strategy of ZnCu-ZIF to synthesize uniform dispersed Zn-Cu pair active sites anchored on nitrogen-doped mesoporous carbon. XPS, EXAFS and KSCN poison experiments reveal the bimetal Zn-N/Cu-N active centers. The DFT calculations confirmed that ZnN_4 and CuN_4 were active sites during ORR. The ZnCu-N-C catalyst exhibits robust ORR activity ($E_{1/2} = 0.87$ V) and durability in 0.1 M KOH. The ZnCu-N-C-based ZAB achieves a power density of 156.2 mW cm^{-2} and robust long-term stability. Experiments and theoretical calculations revealed that the excellent ORR activity is ascribed to the synergistic promotion of Cu-Cu bonds and the uniformly dispersed Zn-N/Cu-N active sites that are beneficial to reducing the oxygen adsorption energy barrier. This work may provide new insight into the preparation and design of M-N$_x$ active sites in high-efficiency Zn-air batteries.

CRediT authorship contribution statement

Mancai Qian: Writing – original draft, Conceptualization. **Man Guo:** Writing – original draft, Conceptualization. **Yuan Qu:** Data curation. **Meijiao Xu:** Data curation. **Datai Liu:** Methodology. **Cheng Hou:** Writing – review & editing. **Tayirjan Taylor Isimjan:** Writing – review & editing. **Xiulin Yang:** Supervision, Writing – review & editing.

Associated content

CCDC 2088187 (I) and 2088196 (II) contain the affiliated crystallographic data, which can be gained free of charge via www.ccdc.cam.ac.uk/data_request/cif.

Declaration of Competing Interest

The authors declare that they have no known competing financial interests or personal relationships that could have appeared to influence the work reported in this paper.

Appendix A. Supporting information

Supplementary data associated with this article can be found in the online version at doi:10.1016/j.jallcom.2022.164527.

References

[1] J. Han, H. Bao, J.-Q. Wang, L. Zheng, S. Sun, Z.L. Wang, C. Sun, 3D N-doped ordered mesoporous carbon supported single-atom Fe-N-C catalysts with superior performance for oxygen reduction reaction and zinc-air battery, Appl. Catal. B: Environ. 280 (2021) 119411.
[2] C. Sun, J.A. Alonso, J. Bian, Recent advances in perovskite-type oxides for energy conversion and storage applications, Adv. Energy Mater. 11 (2021) 2000459.
[3] T. Zhang, J. Bian, Y. Zhu, C. Sun, FeCo nanoparticles encapsulated in N-doped carbon nanotubes coupled with layered double (Co, Fe) hydroxide as an efficient bifunctional catalyst for rechargeable zinc–air batteries, Small 17 (2021) 2103737.
[4] X. Xu, Y. Pan, Y. Zhong, R. Ran, Z. Shao, Ruddlesden–Popper perovskites in electrocatalysis, Mater. Horiz. 7 (2020) 2519–2565.
[5] M.-T.F. Rodrigues, G. Babu, H. Gullapalli, K. Kalaga, F.N. Sayed, K. Kato, J. Joyner, P.M. Ajayan, A materials perspective on Li-ion batteries at extreme temperatures, Nat. Energy 2 (2017) 17108.
[6] J. Han, X. Meng, L. Lu, J. Bian, Z. Li, C. Sun, Single-Atom Fe-N$_x$-C as an efficient electrocatalyst for zinc–air batteries, Adv. Funct. Mater. 29 (2019) 1808872.
[7] Y. Li, H. Dai, Recent advances in zinc–air batteries, Chem. Soc. Rev. 43 (2014) 5257–5275.
[8] Y. Li, M. Gong, Y. Liang, J. Feng, J.-E. Kim, H. Wang, G. Hong, B. Zhang, H. Dai, Advanced zinc-air batteries based on high-performance hybrid electrocatalysts, Nat. Commun. 4 (2013) 1805.
[9] Q. Lai, J. Zheng, Z. Tang, D. Bi, J. Zhao, Y. Liang, Optimal configuration of N-doped carbon defects in 2D turbostratic carbon nanomesh for advanced oxygen reduction electrocatalysis, Angew. Chem. Int. Ed. 59 (2020) 2–10.
[10] J. Luo, X. Qiao, J. Jin, X. Tian, H. Fan, D. Yu, W. Wang, S. Liao, N. Yu, Y. Deng, A strategy to unlock the potential of CrN as a highly active oxygen reduction reaction catalyst, J. Mater. Chem. A 8 (2020) 8575–8585.
[11] X. Meng, J. Han, L. Lu, G. Qiu, Z.L. Wang, C. Sun, Fe^{2+}-doped layered double (Ni, Fe) hydroxides as efficient electrocatalysts for water splitting and self-powered electrochemical systems, Small 15 (2019) 1902551.
[12] D. Li, C. Li, L. Zhang, H. Li, L. Zhu, D. Yang, Q. Fang, S. Qiu, X. Yao, Metal-free thiophene-sulfur covalent organic frameworks: precise and controllable synthesis of catalytic active sites for oxygen reduction, J. Am. Chem. Soc. 142 (2020) 8104–8108.
[13] Y. Chen, S. Ji, S. Zhao, W. Chen, J. Dong, W.-C. Cheong, R. Shen, X. Wen, L. Zheng, A.I. Rykov, S. Cai, H. Tang, Z. Zhuang, C. Chen, Q. Peng, D. Wang, Y. Li, Enhanced oxygen reduction with single-atomic-site iron catalysts for a zinc-air battery and hydrogen-air fuel cell, Nat. Commun. 9 (2018) 5422.
[14] S.-H. Yin, J. Yang, Y. Han, G. Li, L.-Y. Wan, Y.-H. Chen, C. Chen, X.-M. Qu, Y.-X. Jiang, S.-G. Sun, Construction of highly active metal-containing nanoparticles and FeCo-N$_4$ composite sites for the acidic oxygen reduction reaction, Angew. Chem. Int. Ed. 59 (2020) 21976–21979.
[15] Y. Dai, J. Yu, M. Ni, Z. Shao, Rational design of spinel oxides as bifunctional oxygen electrocatalysts for rechargeable Zn-air batteries, Chem Phys. Rev. 1 (2020) 011303.
[16] G. Li, Y. Mu, Z. Huang, N. Wang, Y. Chen, J. Liu, G. Liu, O.L. Li, M. Shao, Z. Shi, Poly-active centric Co$_3$O$_4$-CeO$_2$/Co-N-C composites as superior oxygen reduction catalysts for Zn-air batteries, Sci. China Mater. 64 (2021) 73–84.

[17] X. Zhang, X. Xu, S. Yao, C. Hao, C. Pan, X. Xiang, Z.Q. Tian, P.K. Shen, Z. Shao, S.P. Jiang, Boosting electrocatalytic activity of single atom catalysts supported on nitrogen-doped carbon through N coordination environment engineering, Small (2022) 2105329, https://doi.org/10.1002/smll.202105329

[18] M.Y. Liu, M. Zhang, P. Zhang, Z.P. Xing, B.J. Jiang, Y. Yu, Z. Cai, J.H. Li, J.L. Zou, ZIF-67-derived dodecahedral Co@N-doped graphitized carbon protected by a porous FeS₂ thin-layer as an efficient catalyst to promote the oxygen reduction reaction, ACS Sustain. Chem. Eng. 8 (2020) 4194–4206.

[19] X. Xu, H. Sun, S.P. Jiang, Z. Shao, Modulating metal–organic frameworks for catalyzing acidic oxygen evolution for proton exchange membrane water electrolysis, SusMat 1 (2021) 460–481.

[20] X. Pan, W. Wang, Z. Huang, S. Liu, J. Guo, F. Zhang, H. Yuan, X. Li, F. Liu, H. Liu, MOF-derived double-layer hollow nanoparticles with oxygen generation for multimodal imaging-guided sonodynamic therapy, Angew. Chem. Int. Ed. 59 (2020) 13557–13561.

[21] R.S. Gao, J. Tang, X.L. Yu, S. Tang, K. Ozawa, T. Sasaki, L.C. Qin, In situ synthesis of MOF-derived carbon shells for silicon anode with improved lithium-ion storage, Nano Energy 70 (2020) 104444.

[22] Z.Y. Guo, Z.P. Zhang, Z.L. Li, M.L. Dou, F. Wang, Well-defined gradient Fe/Zn bi-metal organic framework cylinders derived highly efficient iron- and nitrogen-codoped hierarchically porous carbon electrocatalysts towards oxygen reduction, Nano Energy 57 (2019) 108–117.

[23] H.-F. Wang, L. Chen, H. Pang, S. Kaskel, Q. Xu, MOF-derived electrocatalysts for oxygen reduction, oxygen evolution and hydrogen evolution reactions, Chem. Soc. Rev. 49 (2020) 1414–1448.

[24] K. Selvakumar, S.M.S. Kumar, R. Thangamuthu, P. Rajput, D. Bhattacharyya, S.N. Jha, 2D and 3D silica-template-derived MnO₂ electrocatalysts towards enhanced oxygen evolution and oxygen reduction activity, ChemElectroChem 5 (2018) 3980–3990.

[25] D. Wang, B. Su, Y. Jiang, L. Li, B.K. Ng, Z. Wu, F. Liu, Polytype 1T/2H MoS₂ heterostructures for efficient photoelectrocatalytic hydrogen evolution, Chem. Eng. J. 330 (2017) 102–108.

[26] F. Navarro-Pardo, J.B. Liu, O. Abdelkarim, G.S. Selopal, A. Yurtsever, A.C. Tavares, H.G. Zhao, Z.M.M. Wang, F. Rosei, 1D/2D cobalt-based nanohybrids as electrocatalysts for hydrogen generation, Adv. Funct. Mater. 30 (2020) 1908467.

[27] D.S. Liu, M.N. Li, X.C. Li, F.J. Ren, P. Sun, L.C. Zhou, Core-shell Zn/Co MOFs derived Co₃O₄/CNTs as an efficient magnetic heterogeneous catalyst for persulfate activation and oxytetracycline degradation, Chem. Eng. J. 387 (2020) 124008.

[28] P. Yang, Q. Zhang, Z. Yi, J. Wang, H. Yang, Rational electronic control of carbon dioxide reduction over cobalt oxide, J. Catal. 387 (2020) 119–128.

[29] M. Ebrahimi, M. Mansournia, Rapid room temperature synthesis of zeolitic imidazolate framework-7 (ZIF-7) microcrystals, Mater. Lett. 189 (2017) 243–247.

[30] Q. Yu, S. Lian, J. Li, R. Yu, S. Xi, J. Wu, D. Zhao, L. Mai, L. Zhou, FeNₓ and γ-Fe₂O₃ co-functionalized hollow graphitic carbon nanofibers for efficient oxygen reduction in an alkaline medium, J. Mater. Chem. A 8 (2020) 6076–6082.

[31] Y. Lian, K. Shi, H. Yang, H. Sun, P. Qi, J. Ye, W. Wu, Z. Deng, Y. Peng, Elucidation of active sites on S, N codoped carbon cubes embedding Co-Fe carbides toward reversible oxygen conversion in high-performance zinc-air batteries, Small 16 (2020) 1907368.

[32] Z. Hu, Z. Guo, Z. Zhang, M. Dou, F. Wang, Bimetal zeolitic imidazolite framework-derived iron-, cobalt- and nitrogen-codoped carbon nanopolyhedra electrocatalyst for efficient oxygen reduction, ACS Appl. Mater. Interfaces 10 (2018) 12651–12658.

[33] M. Wu, K. Wang, M. Yi, Y. Tong, Y. Wang, S. Song, A facile activation strategy for an MOF-derived metal-free oxygen reduction reaction catalyst: direct access to optimized pore structure and nitrogen species, ACS Catal. 7 (2017) 6082–6088.

[34] F. Pan, B. Li, E. Sarnello, Y. Fei, Y. Gang, X. Xiang, Z. Du, P. Zhang, G. Wang, H.T. Nguyen, T. Li, Y.H. Hu, H.-C. Zhou, Y. Li, Atomically dispersed iron–nitrogen sites on hierarchically mesoporous carbon nanotube and graphene nanoribbon networks for CO₂ reduction, ACS Nano 14 (2020) 5506–5516.

[35] J. Qian, T. Wang, Z. Zhang, Y. Liu, J. Li, D. Gao, Engineered spin state in Ce doped LaCoO₃ with enhanced electrocatalytic activity for rechargeable Zn-Air batteries, Nano Energy 74 (2020) 104948.

[36] S. Dilpazir, R. Liu, M. Yuan, M. Imran, Z. Liu, Y. Xie, H. Zhao, G. Zhang, Br/Co/N Co-doped porous carbon frameworks with enriched defects for high-performance electrocatalysis, J. Mater. Chem. A 8 (2020) 10865–10874.

[37] G. Ye, K. Zhao, Z. He, R. Huang, Y. Liu, S. Liu, Fe-Nₓ sites enriched carbon micropolyhedrons derived from Fe-doped zeolitic imidazolate frameworks with reinforced Fe-N coordination for efficient oxygen reduction reaction, ACS Sustain. Chem. Eng. 6 (2018) 15624–15633.

[38] R.S. Donghui Guo, Chisato Akiba, Shunsuke Saji, Takahiro Kondo, Junji Nakamura, Active sites of nitrogen-doped carbon materials for oxygen reduction reaction clarified using model catalysts, Science 351 (2016) 361–365.

[39] F. Li, Y. Bu, G.-F. Han, H.-J. Noh, S.-J. Kim, I. Ahmad, Y. Lu, P. Zhang, H.Y. Jeong, Z. Fu, Q. Zhong, J.-B. Baek, Identifying the structure of Zn-N₂ active sites and structural activation, Nat. Commun. 10 (2019) 2623.

[40] J. Zang, F.T. Wang, Q.Q. Cheng, G.L. Wang, L.S. Ma, C. Chen, L.J. Yang, Z.Q. Zou, D.Q. Xie, H. Yang, Cobalt/zinc dual-sites coordinated with nitrogen in nanofibers enabling efficient and durable oxygen reduction reaction in acidic fuel cells, J. Mater. Chem. A 8 (2020) 3686–3691.

[41] H.Q. Wang, L.L. Wei, J.T. Liu, J.Q. Shen, Hollow bimetal ZIFs derived Cu/Co/N co-coordinated ORR electrocatalyst for microbial fuel cells, Int. J. Hydrogen Energy 45 (2020) 4481–4489.

[42] S. Ma, Z. Han, K. Leng, X. Liu, Y. Wang, Y. Qu, J. Bai, Ionic exchange of metal-organic frameworks for constructing unsaturated copper single-atom catalysts for boosting oxygen reduction reaction, Small 16 (2020) 2001384.

[43] F. Li, Y. Bu, G.F. Han, H.J. Noh, S.J. Kim, I. Ahmad, Y. Lu, P. Zhang, H.Y. Jeong, Z. Fu, Q. Zhong, J.B. Baek, Identifying the structure of Zn-N₂ active sites and structural activation, Nat. Commun. 10 (2019) 2623.

[44] T. Sun, Y. Li, T. Cui, L. Xu, Y.-G. Wang, W. Chen, P. Zhang, T. Zheng, X. Fu, S. Zhang, Z. Zhang, D. Wang, Y. Li, Engineering of coordination environment and multi-scale structure in single-site copper catalyst for superior electrocatalytic oxygen reduction, Nano Lett. 20 (2020) 6206–6214.

[45] Z. Guo, Z. Zhang, Z. Li, M. Dou, F. Wang, Well-defined gradient Fe/Zn bimetal organic framework cylinders derived highly efficient iron- and nitrogen- codoped hierarchically porous carbon electrocatalysts towards oxygen reduction, Nano Energy 57 (2019) 108–117.

[46] M. Tong, F. Sun, Y. Xie, Y. Wang, Y. Yang, C. Tian, L. Wang, H. Fu, Operando co-operated catalytic mechanism of atomically dispersed Cu−N₄ and Zn−N₄ for promoting oxygen reduction reaction, Angew. Chem. Int. Ed. 60 (2021) 14005–14012.

[47] X.B. Zhang, X. Han, Z. Jiang, J. Xu, L.N. Chen, Y.K. Xue, A.M. Nie, Z.X. Xie, Q. Kuang, L.S. Zheng, Atomically dispersed hierarchically ordered porous Fe-N-C electrocatalyst for high performance electrocatalytic oxygen reduction in Zn-Air battery, Nano Energy 71 (2020) 104547.

[48] F. Li, G.-F. Han, H.-J. Noh, S.-J. Kim, Y. Lu, H.Y. Jeong, Z. Fu, J.-B. Baek, Boosting oxygen reduction catalysis with abundant copper single atom active sites, Energy Environ. Sci. 11 (2018) 2263–2269.

[49] H. Zhong, C. Shi, J. Li, R. Yu, Q. Yu, H. Liu, Y. Yao, J. Wu, L. Zhou, L. Mai, Cobalt decorated nitrogen-doped carbon bowls as efficient electrocatalysts for the oxygen reduction reaction, Chem. Commun. 56 (2020) 4488–4491.

[50] W. Cheng, Z.-P. Wu, D. Luan, S.-Q. Zang, X.W.D. Lou, Synergetic cobalt-copper-based bimetal-organic framework nanoboxes toward efficient electrochemical oxygen evolution, Angew. Chem. Int. Ed. 60 (2021) 26397–26402.

[51] X. Wen, H. Qi, Y. Cheng, Q. Zhang, C. Hou, J. Guan, Cu nanoparticles embedded in N-doped carbon materials for oxygen reduction reaction, Chin. J. Chem. 38 (2020) 941–946.

[52] Z. Li, T. Yang, Z. Zhao, T. Xu, L. Wei, J. Feng, X. Yang, H. Ren, M. Wu, Structural modulation of Co catalyzed carbon nanotubes with Cu-Co bimetal active center to inspire oxygen reduction reaction, ACS Appl. Mater. Interfaces 11 (2019) 3937–3945.

[53] Z. Lu, B. Wang, Y. Hu, W. Liu, Y. Zhao, R. Yang, Z. Li, J. Luo, B. Chi, Z. Jiang, M. Li, S. Mu, S. Liao, J. Zhang, X. Sun, An isolated zinc–cobalt atomic pair for highly active and durable oxygen reduction, Angew. Chem. Int. Ed. 58 (2019) 2622–2626.